Received 1 August 2023; revised 26 August 2023; accepted 9 September 2023. Date of publication 13 September 2023; date of current version 3 October 2023.

Digital Object Identifier 10.1109/OJAP.2023.3314770

Broadband Multi-Shaped Metasurface Circularly Polarized Antenna With Suppressed Non-CP Radiation Modes

NATHAPAT SUPREEYATITIKUL [1] (Member, IEEE), TITIPONG LERTWIRIYAPRAPA [2] (Senior Member, IEEE), NONCHANUTT CHUDPOOTI [3] (Member, IEEE), MONAI KRAIRIKSH [4] (Senior Member, IEEE), AND CHUWONG PHONGCHAROENPANICH [4] (Member, IEEE)

[1]Aeronautical Engineering Division, Civil Aviation Training Center, Bangkok 10900, Thailand
[2]Research Center of Innovation Digital and Electromagnetic Technology, Department of Teacher Training in Electrical Engineering, Faculty of Technical Education, King Mongkut's University of Technology North Bangkok, Bangkok 10800, Thailand
[3]Research Center of Innovation Digital and Electromagnetic Technology, Department of Industrial Physics and Medical Instrumentation, Faculty of Applied Science, King Mongkut's University of Technology North Bangkok, Bangkok 10800, Thailand
[4]School of Engineering, King Mongkut's Institute of Technology Ladkrabang, Bangkok 10520, Thailand

CORRESPONDING AUTHOR: C. PHONGCHAROENPANICH (e-mail: chuwong.ph@kmitl.ac.th)

This work was supported in part by the National Science, Research and Innovation Fund (NSRF) and in part by the King Mongkut's University of Technology North Bangkok under Contract KMUTNB-FF-65-42.

ABSTRACT In this research, a multi-shaped metasurface broadband circularly polarized (CP) patch antenna with parasitic elements is proposed for 5G new radio (NR) applications. The proposed metasurface CP patch antenna comprises triple-layered substrates without air gap. The upper layer sits with multi-shaped metasurface elements and parasitic patches. The middle layer consists of an L-shaped slot functioning as the ground plane, and the lower layer contains a microstrip and a fan-shaped stub functioning as the feed line. The proposed metasurface CP patch antenna with parasitic elements is evaluated using characteristic mode analysis (CMA). The CMA results indicate that the modal significance of Modes 1 and 2 of the multi-shaped metasurface CP antenna are orthogonal, giving rise to circular polarization. The non-CP radiation of Modes 3 and 4 are suppressed by using the multi-shaped metasurface elements and parasitic patches. The measured impedance bandwidth and axial ratio bandwidth are 42.85% (3.4 – 4.9 GHz) and 38% (3.27 – 4.6 GHz), achieving the maximum gain of 7.23 dBic at 3.7 GHz. The experiments demonstrate that the multi-shaped metasurface CP patch antenna with parasitic elements is suitable for 5G NR wireless applications. The novelty of this study is attributed to its utilization of multi-shaped metasurface elements and parasitic patches, which effectively suppress non-circularly polarized radiation modes.

INDEX TERMS Characteristic mode analysis, impedance, metasurfaces, patch antennas, substrates.

I. INTRODUCTION

THE MID-BAND frequency band (1 GHz – 6 GHz) is enabled for 5G new radio (NR) wireless communication because of its extensive coverage and penetrability [1], [2]. As a result, the sub-6 GHz 5G NR technology is adopted in many wireless applications, including cellular networks, satellite communication, remote sensing, and Internet of Things [3], [4], [5], and [6].

Circular polarization is a type of electromagnetic wave polarization in which the electric field vectors rotate in a circular motion as it propagates through space [7]. The rotation is either clockwise or counterclockwise. Circularly polarized (CP) waves are less susceptible to multipath interference and losses, making the CP waves suitable for wireless communication applications [8].

Characteristic mode analysis (CMA) is a methodology employed to assess the current distribution and radiation patterns of antennas [9]. In addition, CMA is used to determine the antenna configuration and dimension, based on the total surface current on a perfect electric conductor.

In modern antennas, metasurface CP patch antennas are deployed in a variety of applications [10], [11], and [12]. The metasurface CP antenna structure typically consists of periodic elements of thin metal sheet in subwavelength and external sources (e.g., microstrip feed line or aperture-coupled feed). The metasurface CP antennas are compact, lightweight, and easy to fabricate. Besides, various shapes of periodic metasurface elements are proposed to convert linearly polarized waves into CP waves [10], [11], [12].

In [10], CP patch antenna with an S-shaped metasurface structure was proposed for C-band uplink applications. The patch antenna achieved an impedance bandwidth (IBW) of 43.22%, covering 4.05 – 6.6 GHz; and axial ratio bandwidth (ARBW) of 22%, covering 5.3 – 6.6 GHz. In [11], a four-cluster metasurface CP array antenna was proposed for C-band small satellites. The array antenna achieved an IBW of 84.74%, covering 4 – 9 GHz, and ARBW of 57.6% for the frequency bands that fall within the range of 4.2 – 7.6 GHz. In [12], an asymmetric metasurface CP microstrip antenna could achieve an IBW of 15.7% (1.58 – 1.85 GHz) and ARBW of 13% (1.58 – 1.8 GHz). However, none of these research works use the CMA technique to realize the CP radiation.

In [13], a four-cluster CP patch antenna array with leaf-shaped metasurface structure characterized by CMA could achieve an IBW of 62.5% (from 3.4 GHz to 5.9 GHz) and ARBW of 21% (from 3.8 GHz to 4.54 GHz). In [14], a CMA-characterized H-shaped metasurface CP patch antenna was proposed for C-band communication. The patch antenna achieved an IBW of 38.8% within the frequency range of 4.42 – 6.55 GHz, and ARBW of 14.3% occurring the spectrum range of 5.2 – 6 GHz. In [15], a CMA-characterized irregular-shaped metasurface CP antenna array was proposed for C- and X-band applications. The antenna array achieved an IBW of 49.6%, occurring the frequency between 6.23 – 10.37 GHz, and ARBW of 33.13% between the spectrum range from 7 GHz to 9.78 GHz. However, no attempts have been made to suppress the non-CP radiation modes, resulting in narrow ARBW.

This research thus proposes a broadband multi-shaped CP patch antenna with parasitic elements for 5G NR wireless technology. The proposed multi-shaped metasurface patch antenna is defined by CMA. The non-CP radiation modes are suppressed by using multi-shaped metasurface elements and parasitic patches. The feed structure is made up of an L-shaped slot ground plane and a microstrip feed line, exciting the CP modes. Simulations are performed using CST Studio Suite and experimented carried out with an antenna prototype. The performance metrics of the broadband CMA-characterized multi-shaped metasurface CP patch antenna with parasitic elements include the antenna gain, impedance bandwidth ($|S_{11}| \leq -10$ dB), axial ratio bandwidth (AR ≤ 3 dB), and radiation patterns.

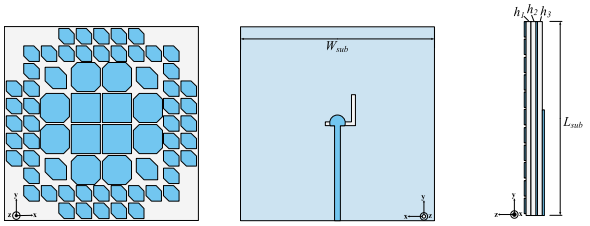

FIGURE 1. Configuration of the proposed CMA-characterized multi-shaped metasurface CP patch antenna with parasitic elements: (a) front view, (b) rear view, (c) side view.

II. ANTENNA DEVELOPMENT METHODOLOGY

A. MULTI-SHAPED METASURFACE CP PATCH ANTENNA WITH PARASITIC ELEMENTS

Figures 1(a)-(c) show the front, rear, and side views of the CMA-characterized multi-shaped metasurface CP patch antenna with parasitic elements. The proposed patch antenna comprises a triple-layered FR-4 substrate (without air gap), stacking as an upper layer; middle layer; and lower layer. The dimensions of the triple-layered substrate are 100 mm $\times$ 100 mm ($W_{sub} \times L_{sub}$). The thickness and dielectric constant of the FR-4 substrate are 1.6 mm (h_1, h_2, h_3) and 4.3 (ε_r).

The upper layer contains multi-shaped metasurface elements and parasitic elements (i.e., corner-truncated square-shaped patches). The multi-shaped metasurface includes four square-shaped metasurface elements, eight octagonal-shaped metasurface elements, and four corner-truncated square-shaped metasurface elements. The middle layer contains an L-shaped slot that functions as the ground plane. On the lower layer sits a microstrip and a fan-shaped stub functioning as the feed line. The stub is utilized to enable impedance matching.

B. THEORY OF CHARACTERISTIC MODES

The theory of characteristic mode analysis (CMA) is used to define the configuration and dimension of the antenna parameters, characterizing the resonant frequency [16]. The CMA utilizes the entire surface current on the perfect electric conductor (PEC) structure. The entire surface current ($J(\omega)$) on the PEC structure is evaluated by equation (1) [17].

$$J(\omega) = \sum_{n=1}^{N} \alpha_n(\omega) J_n(\omega) \tag{1}$$

where $\alpha(\omega)$ is the modal weighting coefficient (MWC), $J(\omega)$ is the characteristic current, and N is the number of modes.

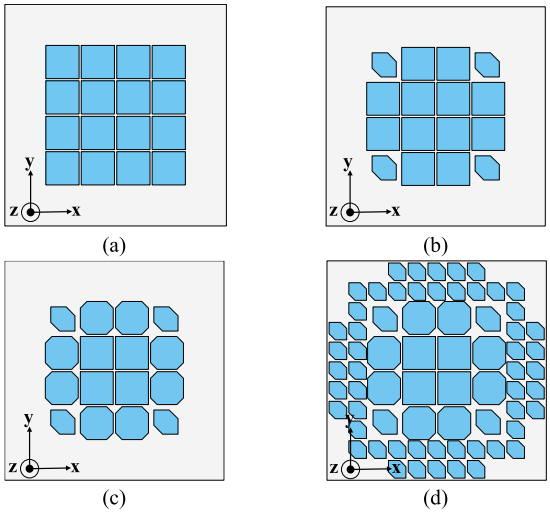

FIGURE 2. Development procedures of the proposed multi-shaped metasurface CP patch antenna with parasitic elements: (a) Model-I, (b) Model-II, (c) Model-III, (d) Model-IV.

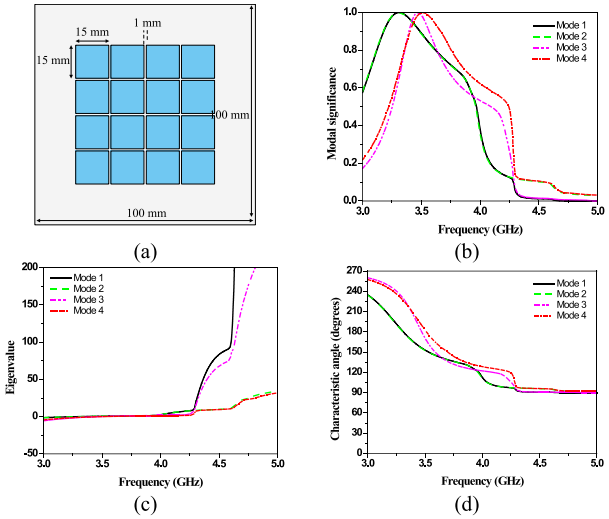

FIGURE 3. The 4 × 4 square-shaped metasurface elements on a lossless FR-4 substrate (i.e., Model-I): (a) geometry, (b) the simulated MS, (c) the simulated eigenvalue, (d) the simulated CA.

The MWC is calculated by equation (2) [18].

$$\alpha_n(\omega) = \frac{v_n^i(\omega)}{1 + j\lambda_n(\omega)} \tag{2}$$

where $\lambda_n(\omega)$ is the characteristic eigenvalue and $v_n^i(\omega)$ is the modal excitation coefficient (MEC), which is calculated by equation (3) [19].

$$v_n^i(\omega) = \left\langle J_n(\omega), E^i(\omega) \right\rangle = \iint_s J_n(\omega) \cdot E^i(\omega)\ \mathrm{ds} \tag{3}$$

where E^i is the surface area excitation on the PEC structure.

The modal significance (MS $\geq$ 0.707) is well-known to represent the characteristic current ($J(\omega)$) and antenna radiation modes. The phases difference between two orthogonal modes are investigated by characteristic angle (CA). The MS of two orthogonal modes must be identical and their CA is approximately ±90° to realize the CP radiation. Equations (4) and (5) are used to evaluate the MS and CA [20].

$$\mathrm{MS} = \left| \frac{1}{1 + j\lambda_n(\omega)} \right| \tag{4}$$

$$\mathrm{CA} = 180^\circ - \tan^{-1}(\lambda_n(\omega)) \tag{5}$$

C. DEVELOPMENT PROCEDURES OF METASURFACE SCHEMES

The antenna design was simulated using CST Multilayer Solver. Four development procedures (i.e., Model-I, Model-II, Model-III, and Model-IV) of the proposed multi-shaped metasurface CP patch antenna with parasitic elements were shown in Figures 2(a)-(d). In Model-I, 4 × 4 square-shaped metasurface elements (15 mm × 15 mm) are placed on a lossless FR-4 substrate. The substrate dimension is 100 mm × 100 mm and 3.2 mm in thickness. In Model-II, the square-shaped metasurface elements at the four corners are truncated to obtain corner-truncated square-shaped metasurface elements (11 mm × 11 mm). In Model-III, the lateral metasurface elements are transformed into the metasurface elements of octagonal shape (15 mm × 15 mm). In Model-IV, the Model-III scheme is surrounded by corner-truncated square-shaped elements (the parasitic elements; 8 mm × 8 mm).

Figure 3(a) shows the geometry of Model-I, Figure 3(b) presents the simulated modal significance (MS) of Model-I, Figure 3(c) presents the simulated eigenvalue of Model-I, and Figure 3(d) presents the simulated characteristic angle (CA) of Model-I. The simulated MS of Modes 1 – 4 of Model-I are equal to 1 at 3.31 GHz, 3.31 GHz, 3.47 GHz, 3.51 GHz, achieving the resonant frequency between 3.3 – 3.51 GHz, as shown in Figure 3(b). In Figure 3(c), the eigenvalues of Modes 1 – 4 of Model-I are almost 0 for resonate mode between 3 – 4.3 GHz. In Modes 2 and 4, the eigenvalues between 4.3 – 5 GHz are slightly increased while Modes 1 and 3 sharply increased. As a result, Modes 1 – 4 could generate the resonant frequency between 3 – 4.3 GHz. Thus, the eigenvalues of Mode 1 between 4.3 – 5 GHz could be 0 for resonant frequency bandwidth enhancement and CP radiation. The phase differences of Modes 1&2 and 3&4 of simulated CA are almost 0°, as shown in Figure 3(d). The simulated CA of Model-1 failed to achieve the 90° phase difference. To further validate, the magnitude of the modal 3D radiation patterns and surface current distribution between Modes 1 and 2 of Model-I must be identical with orthogonal phase to realize the CP radiation.

Figures 4(a)-(b) show the exemplary surface current distribution and the modal 3D radiation patterns of Model-I at 3.3 GHz. The surface current of Modes 1 and 2 of Model-I flow along the metasurface edges at the center of the metasurface scheme in respectively vertical and horizontal directions, as shown in Figure 4(a). The surface current of Mode 3 is concentrated around the four corners of Model-I,

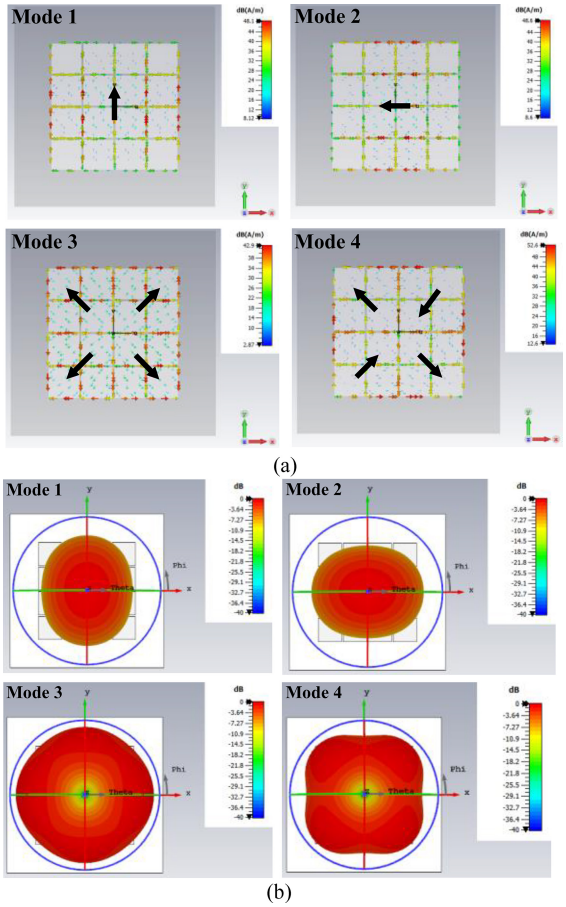

FIGURE 4. Simulated results of Model-I at 3.3 GHz: (a) surface current distribution, (b) modal 3D radiation patterns.

and the surface currents of Mode 4 travel laterally along the outer edges of Model-I. The surface current of Mode 3 is concentrated around the four corners of Model-I, and the surface currents of Mode 4 travel laterally along the outer edges of Model-I. Figure 4(b) shows that the 3D radiation patterns of Modes 1 and 2 are both symmetrical with the main lobe pointing in the positive z-direction, while those of Modes 3 and 4 are of null radiation in the +z direction. The 3D radiation patterns of Modes 1 and 2 of Model-I are of circular polarization, resulting in CP radiation.

The surface currents are related to the characteristic current $J(\omega)$ in equation (1), which are represented by MS in equation (4). Besides, the characteristic eigenvalue ($\lambda_n(\omega)$) indicates each mode status: $\lambda_n(\omega) > 0$ is inductance mode; $\lambda_n(\omega) = 0$ is resonant mode; and $\lambda_n(\omega) < 0$ is capacitance mode [21]. To suppress the resonant mode of Modes 3 and 4 (non-CP radiation modes), the characteristic eigenvalue must not equal 0 between specific frequency ranges. Thus, the surrounding parasitic patches are used to reduce the surface currents on the multi-shaped metasurface elements of Modes 3 and 4.

The MS of non-CP radiation modes (Modes 3 and 4) can be suppressed by manipulating the metasurface elements, with no effect on the CP radiation modes (Modes 1 and

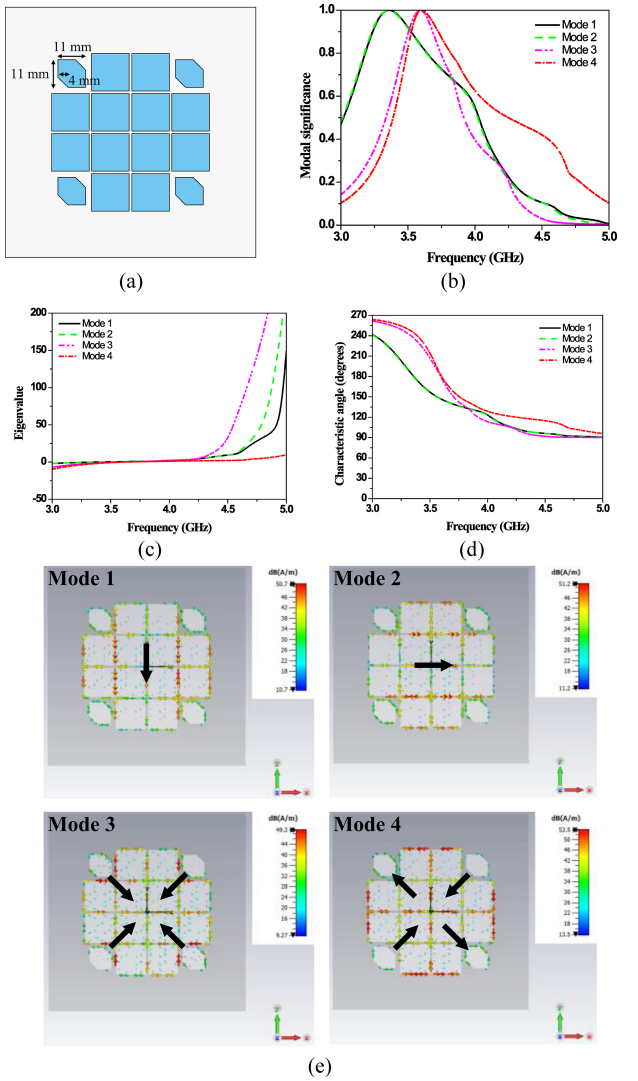

FIGURE 5. Simulated results of Model-II: (a) geometry, (b) MS, (c) eigenvalue, (d) CA, (e) surface current distribution at 3.5 GHz.

2). First, the metasurface elements at the four corners are truncated into corner-truncated metasurface elements (Model-II). Next, the lateral metasurface elements are transformed into the metasurface elements of octagonal shape (Model-III). Then, the multi-shaped metasurface elements are surrounded by corner-truncated square-shaped elements or parasitic elements (Model-IV).

Figure 5(a) illustrates the geometry of Model-II, where the metasurface elements at the four corners are truncated into the corner-truncated metasurface elements. The simulated MS of Modes 1 – 4 are all equal to 1 at 3.36 GHz, 3.35 GHz, 3.59 GHz, and 3.6 GHz (Figure 5(b)). This indicates that the antenna resonant frequency is between 3.35 – 3.6 GHz. The simulated MS of Modes 3 and 4 of Model-II slightly shift to higher frequency (from originally 3.47 GHz and 3.51 GHz for Model-I to 3.59 GHz and 3.6 GHz for Model-II).

In Figure 5(c), The eigenvalues of Modes 1 – 4 in Model-II exhibit values close to zero, indicating resonance occurring between the frequency range of 3 – 4.3 GHz. In Mode 1, the

eigenvalue is decreased (almost 0) between 4.3 – 4.6 GHz while in Mode 2 is negligible increased. As a result, Modes 1 and 2 could generate CP radiation between 3 – 4.6 GHz. On the other hand, Mode 4 is almost 0 between 4.3 – 4.6 GHz, giving rise to non-CP resonant mode interference. Thus, Mode 4 must be suppressed by reducing surface currents. In Figure 5(d), the phase differences between Modes 1 and 2 of simulated CA are 0°. Meanwhile, the surface currents around the metasurface elements at the four corners of Model-II at 3.5 GHz (the center frequency) are substantially decreased, as shown in Figure 5(e).

Figure 6(a) shows the geometry of Model-III. The MS of Mode 4 is suppressed by transforming four pairs of the lateral metasurface elements into the octagonal-shaped metasurface elements. The simulated MS of Modes 1 – 4 are all equal to 1 at frequencies of 3.45 GHz, 3.44 GHz, 3.74 GHz, and 3.76 GHz, as shown in Figure 6(b). This means that the antenna resonant frequency is between 3.44 and 3.76 GHz. The simulated MS of Modes 3 and 4 shift to higher frequency (from originally 3.59 GHz and 3.6 GHz for Model-II to 3.74 GHz and 3.76 GHz for Model-III).

In Figure 6(c), the eigenvalues of Modes 1 – 4 in Model-III are nearly 0 which indicates resonance frequency between 3.3 – 4.4 GHz. The eigenvalues of Mode 4 are sharply increased between 4.4 – 5 GHz for resonant mode suppression. Meanwhile, the eigenvalues of Mode 3 declined rapidly. Thus, Mode 3 should be further suppressed. The phase differences between Modes 1 and 2 of simulated CA are 0°, as shown in Figure 6(d). In Figure 6(e), the surface currents around the lateral octagonal-shaped metasurface elements of Model-III at 3.5 GHz are significantly decreased.

Figure 7(a) shows the geometry of Model-IV. The surrounding parasitic elements are used to further suppress the surface current of Modes 3 and 4. The simulated MS of Modes 1 – 4 are all equal to 1 at 3.45 GHz, 3.44 GHz, 3.68 GHz, and 3.75 GHz, as shown in Figure 7(b). The antenna resonant frequency is between 3.44 and 3.75 GHz, as indicated by the simulated MS (Modes 1 – 4). The simulated MS (Modes 3 and 4) of Model-IV slightly shifts to higher frequency (from originally 3.74 GHz and 3.68 GHz for Model-III to 3.76 GHz and 3.75 GHz for Model-IV).

In Figure 7(c), the eigenvalues of Modes 1 – 4 of Model-IV are rather steady (nearly 0) between 3.5 – 4.3 GHz for resonant modes. The eigenvalues of Modes 3 and 4 are sharply increased between 4.4 – 5 GHz because of the surrounding parasitic elements. As a result, the CP radiation modes (Modes 1 and 2) could be attained within 3 – 4.6 GHz of the frequency ranges. The phase difference between Modes 1 and 2 of simulated CA is 0°, as shown in Figure 7(d).

In Figure 7(e), the parasitic elements reduce the surface current around the metasurface elements at the four corners (Mode 3) and along the edges of the lateral metasurface elements (Mode 4). To achieve CP radiation, an external source (i.e., L-shaped slot ground plane) must excite Modes 1 and

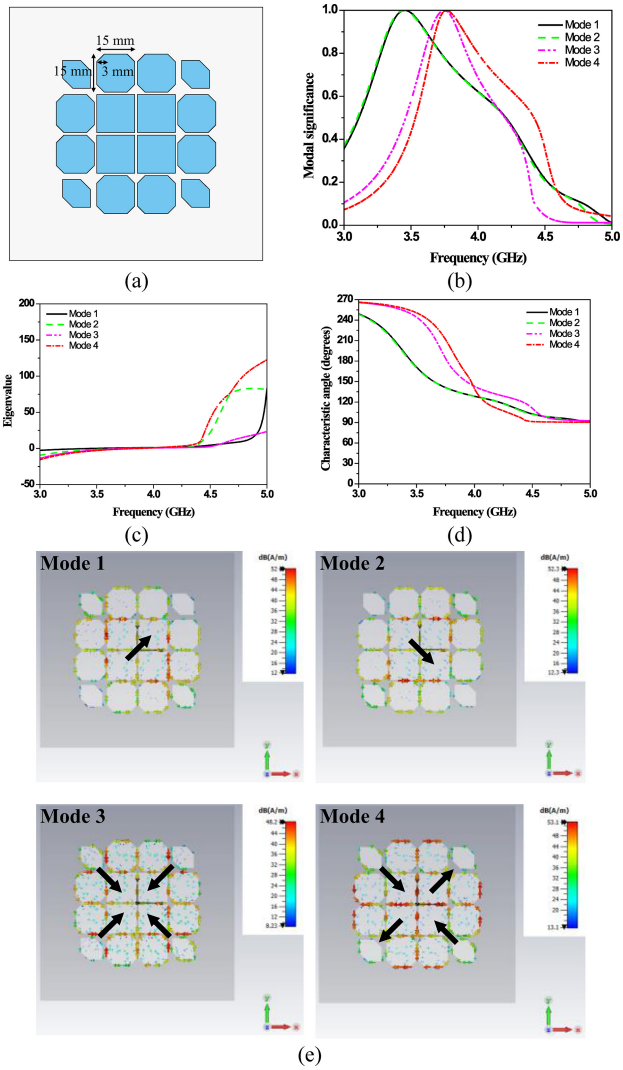

FIGURE 6. Simulated results of Model-III: (a) geometry, (b) MS, (c) eigenvalue, (d) CA, (e) surface current distribution at 3.5 GHz.

2 of the multi-shaped metasurface elements and parasitic patches. Due to the right-hand circular polarization (RHCP), the surface current distribution must be traveled in an orthogonal direction between two modes (Modes 1 and 2) while rotating in a clockwise direction (all-time phase variation). In all scheme models, the current distribution is demonstrated at 0° of the time phase variation.

In Model-IV, the parasitic elements around the metasurface scheme are used to reduce the non-CP modes coupling between the metasurface elements in all directions, while maintaining the two orthogonal modes. The flowing currents from the metasurface elements to parasitic elements generated a high resonant frequency. In comparison, the ARBW difference between Model-III and Model-IV is between 4.12 – 4.61 GHz (Figure 15(b)).

The non-CP radiation modes (Modes 3 and 4) are suppressed by transforming the peripheral metasurface elements and surrounding it with the parasitic elements (i.e., Model-IV). The transformed metasurface elements and the parasitic

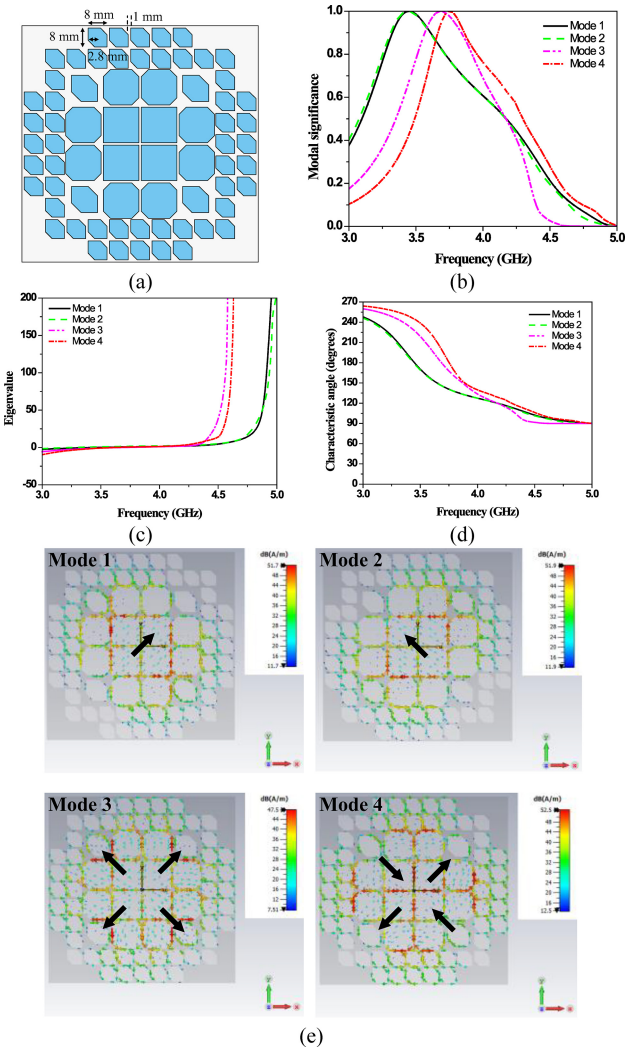

FIGURE 7. Simulated results of Model-IV: (a) geometry, (b) MS, (c) eigenvalue, (d) CA, (e) surface current distribution at 3.5 GHz.

elements suppress the non-CP radiation modes (Modes 3 and 4) and cause the MS of Modes 3 and 4 to shift to higher frequency, resulting in wider ARBW. Furthermore, the number of parasitic elements is determined by a quantity (i.e., as much as possible) of surface current distribution reduction for non-CP radiation modes while the multi-shaped metasurface elements can be given wide IBW ($|S_{11}| \leq$ -10 dB) and ARBW (AR $\leq$ 3 dB).

Figure 8(a) illustrates the L-shaped slot ground plane, and Figure 8 (b) depicts the microstrip feed line. The L-shaped slot sits at the center of the ground plane (middle layer). The dimensions of the horizontal slot ($L_a \times L_{b1}$) and vertical slot ($L_a \times L_{b2}$) are 2 mm × 13.5 mm and 2 mm × 16 mm. The microstrip feed line consists of a feed line ($W_f \times L_f$: 3 mm × 49 mm) and a fan-shaped stub (R: 4 mm). The linearly polarized waves along the X- and Y-axes are generated from the coupling between the microstrip feed line and the L-shaped slot ground plane. To excite the orthogonal modes (Modes 1 and 2), the L-shaped slot on the middle layer

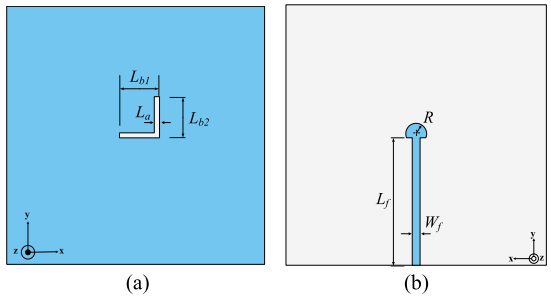

FIGURE 8. Geometry of the feed structure: (a) L-shaped slot ground plane, (b) microstrip feed line.

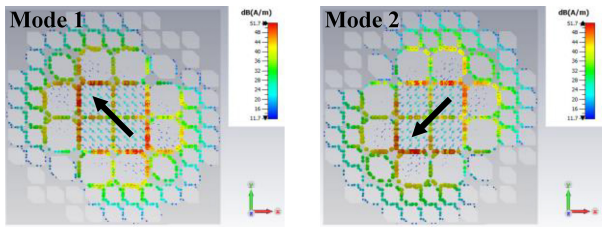

FIGURE 9. Modal magnetic fields of Modes 1 and 2 of Model-IV at the center frequency (3.5 GHz).

must be located underneath the intensive magnetic current of Model-IV.

The magnetic current of Model-IV can be determined by the modal magnetic field. In Figure 9, the intensive modal magnetic field at 3.5 GHz of Modes 1 and 2 of Model-IV. The L-shaped slot excitation is calculated by equation (6) [22].

$$v_n^i = \langle H_n(\omega), M(\omega) \rangle = \iint_s H_n(\omega) \cdot M(\omega)\, ds \tag{6}$$

where $H_n(\omega)$ is the modal magnetic field of the number of n mode and $M(\omega)$ is the magnetic current of the L-shaped slot ground plane.

The parametric study is performed to determine the results of different feed structures on IBW and ARBW of the CMA-characterized multi-shaped metasurface CP patch antenna with parasitic elements. In this research, the feed structure refers to the L-shaped slot ground plane on the middle layer and the microstrip feed line on the lower layer. The parameters being studied include the microstrip feed line length (L_f), the microstrip feed line width (W_f), the width of the L-shaped slot ground plane (L_a), the horizontal length of the L-shaped ground plane (L_{b1}), and the vertical length of the L-shaped ground plane (L_{b2}).

Figures 10(a)-(b) show the simulated IBW and ARBW under different L_f: 46, 49, and 52 mm. In Figure 10(a), IBW fails to cover the sub-6 GHz spectrum for L_f = 46 mm. IBW are between 3.4 – 4.92 GHz for L_f = 49 mm and between 3.2 – 3.48 GHz for L_f = 52 mm. The AR is greater than 3 dB between 4.3 – 4.43 GHz for L_f = 46 mm (Figure 10(b)). ARBW is between 3.29 – 4.61 GHz for L_f = 49 mm and between 3.29 – 4.6 GHz for L_f = 52 mm. The optimal L_f is 49 mm.

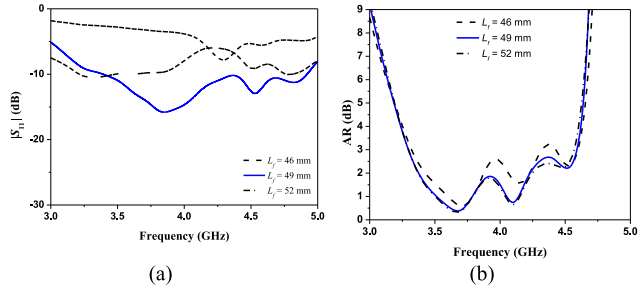

FIGURE 10. Simulated results of Model-IV under different L_f: (a) IBW, (b) ARBW.

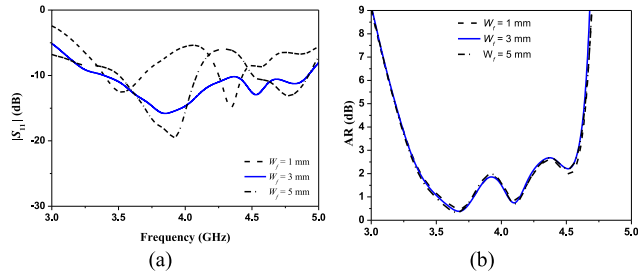

FIGURE 11. Simulated results of Model-IV under different W_f: (a) IBW, (b) ARBW.

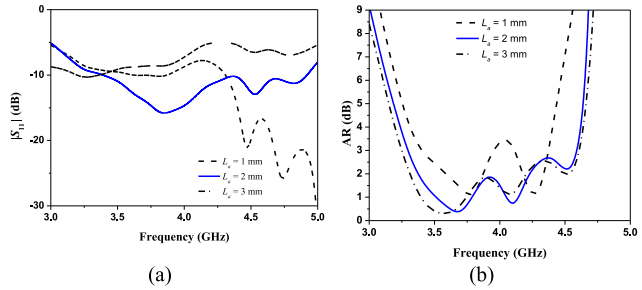

FIGURE 12. Simulated results of Model-IV under different L_a: (a) IBW, (b) ARBW.

The simulated IBW and ARBW under variable W_f (i.e., 1, 3, and 5 mm) are illustrated in Figures 11(a) and (b). In Figure 11(a), given W_f = 1 mm and 5 mm, an impedance mismatch occurs between 3.68 – 4.25 GHz and between 4.08 – 4.5 GHz, respectively. With W_f = 3 mm, IBW is between 3.4 – 4.92 GHz. The optimal W_f is 3 mm. In Figure 11(b), the results also show that W_f has a negligible effect on ARBW of the proposed metasurface CP patch antenna.

The simulated IBW and ARBW under variable L_a (i.e., 1, 2, and 3 mm) are depicted in Figures 12(a) and (b), respectively. As shown in Figure 12(a), IBW are between 3.19 – 3.36 GHz for L_a = 1, between 3.4 – 4.92 GHz for L_a = 2, and between 4.3 – 5 GHz for L_a = 3. In Figure 12(b), AR > 3 dB between 3.94 – 4.12 GHz for L_a = 1 mm. ARBW are between 3.29 – 4.61 GHz for L_a = 2 mm and between 3.25 – 4.62 GHz for L_a = 3 mm. However, L_a = 3 mm results in narrow IBW. The optimal L_a is thus 2 mm.

Figures 13(a)-(b) show the simulated IBW and ARBW under variable L_{b1}: 10.5, 13.5, and 16.5 mm. In Figure 13(a), with L_{b1} = 10.5 mm, IBW fails to cover the sub-6 GHz 5G

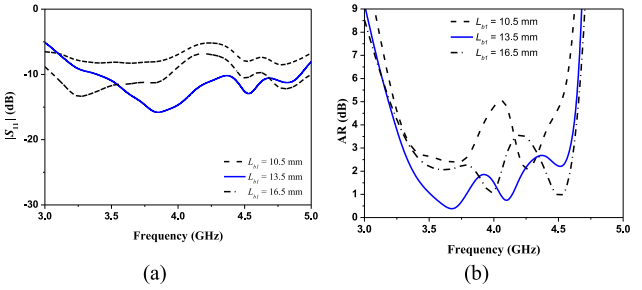

FIGURE 13. Simulated results of Model-IV under variable L_{b1}: (a) IBW, (b) ARBW.

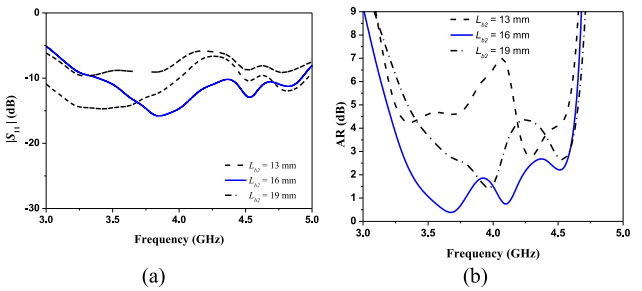

FIGURE 14. Simulated results of Model-IV under variable L_{b2}: (a) IBW, (b) ARBW.

frequency spectrum. Given L_{b1} = 16.5 mm, $|S_{11}| > -10$ dB between 3.93 – 4.45 GHz and between 4.56 – 4.65 GHz. With L_{b1} = 13.5 mm, IBW covers 3.4 – 4.92 GHz. In Figure 13(b), AR > 3 dB between 3.83 – 4.17 GHz for L_{b1} = 10.5 and between 4.1 – 4.31 GHz for L_{b1} = 16.5 mm. The ARBW is between 3.29 – 4.61 GHz for L_{b1} = 13.5 mm. The optimal L_{b1} is 13.5 mm.

The simulated IBW and ARBW under variable L_{b2} (13, 16, and 19 mm) are illustrated in Figures 14(a) and (b), respectively. As shown in Figure 14(a), given L_{b2} = 13 mm, $|S_{11}| > -10$ dB between 4 – 4.48 GHz and 4.57 – 4.68 GHz. IBW failed to cover the sub-6 GHz 5G frequency spectrum for L_{b2} = 19 mm. The IBW is between 3.4 – 4.92 GHz for L_{b2} = 16 mm. In Figure 14(b), with L_{b2} = 13 mm, ARBW is very narrow (4.22 – 4.34 GHz). AR is greater than 3 dB between 4.07 – 4.46 GHz for L_{b2} = 16 mm. With L_{b2} = 16 mm, ARBW is between 3.29 – 4.61 GHz. The optimal L_{b2} is 16 mm.

The simulated IBW, ARBW and gain of Model-I, Model-II, Model-III, and Model-IV with the feed structure are shown in Figures 15(a)-(c), respectively. In Figure 15(a), the simulated IBW of Model-I and Model-II at 3.5 GHz are 33.42% (3.35 – 4.52 GHz) and 33.71% (3.4 – 4.58 GHz), respectively. However, $|S_{11}| > -10$ dB between 4.52 – 4.62 GHz for Model-I and between 4.58 – 4.73 GHz for Model-II. The IBW of Model-III and Model-IV at 3.5 GHz are 43.14% (3.46 – 4.97 GHz) and 43.71% (3.39 – 4.92 GHz), respectively. The IBW of Model-IV is slightly wider than Model-III.

The simulated ARBW of Model-I, Model-II, Model-III, and Model-IV at 3.5 GHz are 10.85% (3.18 – 3.56 GHz), 20.31% (3.18 – 3.89 GHz), 24% (3.28 – 4.12 GHz), and

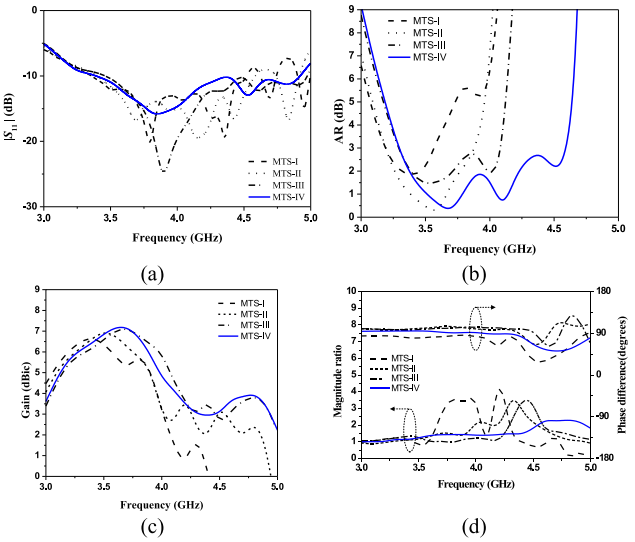

FIGURE 15. Simulated results of Model-I, Model-II, Model-III, and Model-IV with the feed structure: (a) IBW, (b) ARBW, (c) gain, (d) magnitude ratio and phase difference.

37.71% (3.29 – 4.61 GHz), respectively (Figure 15(b)). In Model-II, ARBW becomes wider than that of Model-I. In Model-III, ARBW slightly shifts to higher frequency and becomes wider, compared to Model-II. In Model-IV, ARBW becomes wider than that of Model-III, resulting in broader ARBW.

In comparison, the corner-truncated square-shaped metasurface elements (Model-II) and the octagonal-shaped metasurface elements (Model-III) have an effect on high frequency due to the size reduction of the metasurface elements, giving rise to the S_{11} and ARBW changed. However, IBW ($|S_{11}| \leq -10$ dB) and ARBW (AR $\leq$ 3 dB) have become wider at the high-frequency range.

In Figure 15(c), the simulated gains of Model-I, Model-II, Model-III, and Model-IV are 6.71, 7.05, 7.15, and 7.2 dBic at 3.4, 3.5, 3.7, and 3.7 GHz, respectively. The transformed metasurface elements and the surrounding parasitic elements cause the maximum gain of Model-II, Model-III, and Model-IV to shift to high frequency. In Model-IV, the surrounding parasitic elements have minimal effect on the maximum gain. Table 1 organizes the dimension parameters of the proposed CMA-characterized multi-shaped metasurface CP patch antenna with parasitic elements.

The simulated IBW, ARBW, gain, and electric field of Model-I, Model-II, Model-III, and Model-IV with the feed structure are shown in Figures 15(a)-(d), respectively. To further investigate the CP radiation, the phase difference ($\angle E_x - \angle E_y$) and the magnitude ratio ($|E_x|/|E_y|$) of the electric field are ±90° and 1 [23]. In Figure 15(d), the phase difference of Model-I, Model-II, Model-III, and Model-IV are almost ±90° between 3 – 4.5 GHz of the frequency range. Meanwhile, the magnitude ratio of Model-I, Model-II, Model-III, and Model-IV are approximately 1 between 3 – 3.6 GHz, 3 – 3.8 GHz, 3 – 4.25 GHz, and 3 – 4.5 GHz, respectively. As a result, Model-IV achieved 1 magnitude ratio and 90° phase difference which corresponds to ARBW (AR $\leq$ 3 dB) for wideband CP radiation (Figure 15(b)).

TABLE 1. The dimension parameters of the proposed CMA-characterized multi-shaped metasurface CP patch antenna with parasitic elements.

Parameters	W_{sub}	L_{sub}	h_1	h_2	h_3	L_f
Values (mm)	100	100	1.6	1.6	1.6	49
Parameters	W_f	R	L_a	L_{b1}	L_{b2}	
Values (mm)	3	4	2	13.5	16	

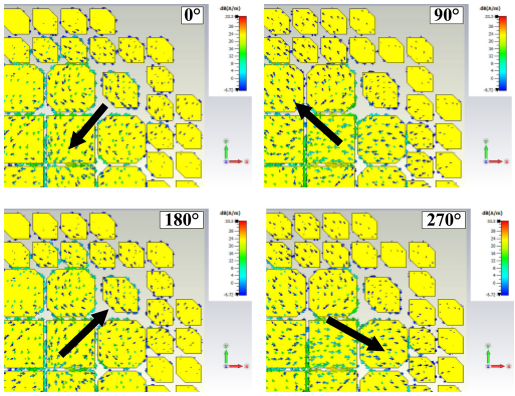

FIGURE 16. Surface current distribution of the proposed CP patch antenna with parasitic elements at 3.5 GHz.

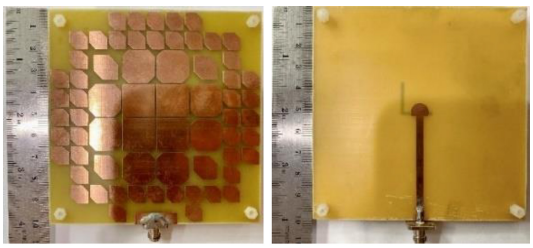

FIGURE 17. Prototype antenna of the proposed CMA-characterized multi-shaped metasurface CP antenna with parasitic elements: (a) front view, (b) rear view.

The current distribution (center frequency) of the proposed metasurface CP patch antenna with parasitic elements is shown at four different phases: 0°, 90°, 180°, and 270° (Figure 16). Specifically, the electric field vectors on the multi-shaped metasurface elements and the parasitic elements traverse clockwise (right-hand circular polarization) in the +z direction.

Figures 17 show the prototype antenna of the proposed multi-shaped metasurface CP patch antenna with parasitic elements. Due to the fabrication limitations, the three outermost parasitic elements (upper layer) are replaced with ground plane to connect with an SMA connector (Figure 17(a)). Polytetrafluoroethylene (PTFE) Teflon spacers are used to secure the triple-layered substrates without air gap.

III. EXPERIMENTAL RESULTS

The prototype antenna performances were measured in an anechoic chamber, which used a vector network analyzer

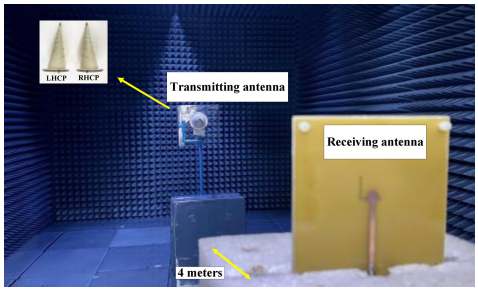

FIGURE 18. The measurement equipment in an anechoic chamber.

(ZNLE6 Rohde & Schwarz). A pair of ETS-Lindgren spiral antenna (3102 model series) and a prototype antenna functioned as transmitting and receiving antennas, respectively. The distance between the antennas was 4 meters [24]. The spiral antennas were used to measure the polarization characteristics (RHCP and LHCP) of the prototype antenna (Figure 18).

The axial ratio (AR) of the prototype antenna was determined by measuring the co-polarized (RHCP) and cross-polarized (LHCP) electric fields between the (prototype antenna), corresponding to $|E_{RHCP}|$ and $|E_{LHCP}|$, respectively. The AR is calculated by equation (7) [25].

$$AR(\text{dB}) = 20\log\left(\frac{|E_{RHCP}| + |E_{LHCP}|}{|E_{RHCP}| - |E_{LHCP}|}\right) \tag{7}$$

where $|E_{RHCP}|$ and $|E_{LHCP}|$ are the electric field magnitudes of the RHCP and LHCP between the spiral and prototype antennas.

Figure 19(a) shows the comparison between simulated and measured IBW of the proposed CMA-characterized multi-shaped metasurface CP patch antenna with parasitic elements. In spite of the similar IBW between simulated and measured results of the proposed CMA-characterized multi-shaped metasurface CP patch antenna with parasitic elements, the S_{11} between simulation and measurement is different within frequency ranges of 3.8 – 4.5 GHz since the replacement of three outermost parasitic elements with a ground plane for the SMA connector.

Figure 19(b) illustrates the simulated and measured ARBW and gain. The simulated and measured results are agreeable. Specifically, the comparison between simulated and measured IBW is 43.4% (3.4 – 4.92 GHz) and 42.85% (3.4 – 4.9 GHz). The simulated and measured ARBW is 37.71% (3.29 – 4.61 GHz) and 38% (3.27 – 4.6 GHz). Moreover, the maximum gain at 3.7 GHz between simulated and measured results is 7.2 dBic and 7.23 dBic. Despite the unstable gain of the antenna, the proposed multi-shaped metasurface CP patch antenna with parasitic elements achieves a 3-dB boresight gain of 22.85% (3.2 – 4 GHz) which corresponded to ARBW of 38% (3.27 – 4.6 GHz) for CP radiation, resulting in the proposed antenna covered the entire the global 5G NR spectrum (3.3 – 4 GHz) [26]. To achieve a stable gain of the metasurface-based CP antenna, the metasurface structure could be symmetrically shaped and

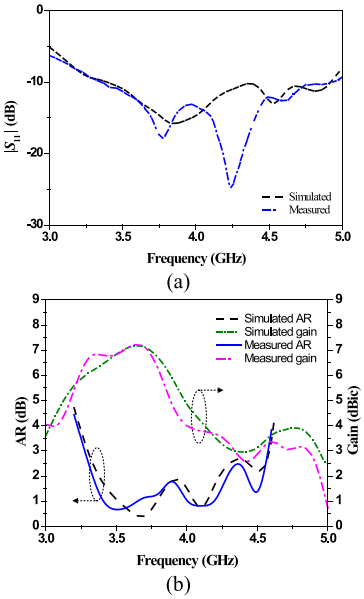

FIGURE 19. Comparison between simulated and measured of IBW, ARBW and gain of the proposed CMA-characterized multi-shaped metasurface CP patch antenna with parasitic elements: (a) IBW, (b) ARBW and gain.

periodically arranged. Besides, the symmetrical-shaped slot ground plane with a feed network could be optimized for achieving CP radiation [27].

In Figures 20(a)-(c), the simulated and measured of the RHCP and LHCP radiation patterns were compared at frequency of 3.5, 4, and 4.5 GHz, respectively. The simulated and measured RHCP and LHCP are in good agreement. The proposed CP patch antenna with parasitic elements is RHCP characteristic (Figure 16). Thus, the co-polarization between transmitting antenna and receiving antenna is RHCP while the cross-polarization is LHCP. In other words, co-polarization (RHCP) refers to the radiation of an antenna in the intended direction (i.e., front of antenna), while cross-polarization is the antenna radiation in undesired directions.

At lower frequencies, the RHCP demonstrates negligible loss in transmission (far-field region), whereas higher frequencies result in substantial transmission loss. As a result, the power radiation difference between RHCP and LHCP is extremely high at low frequencies. On the other hand, the power difference between RHCP and LHCP is decreased at high frequencies.

Table 2 compares the previous metasurface CP patch antennas and the proposed CMA-characterized multi-shaped metasurface CP patch antenna with parasitic elements. In [13], a four-cluster CP patch antenna array with leaf-shaped metasurface structure achieves wide IBW but suffers from narrow ARBW. In [14], CP patch antenna with H-shaped metasurface structure has high antenna gain but its ARBW is narrow. In [15], CP patch antenna array with irregular rectangular-shaped metasurface structure achieves wide IBW, ARBW, and high gain. However, it also suffers from

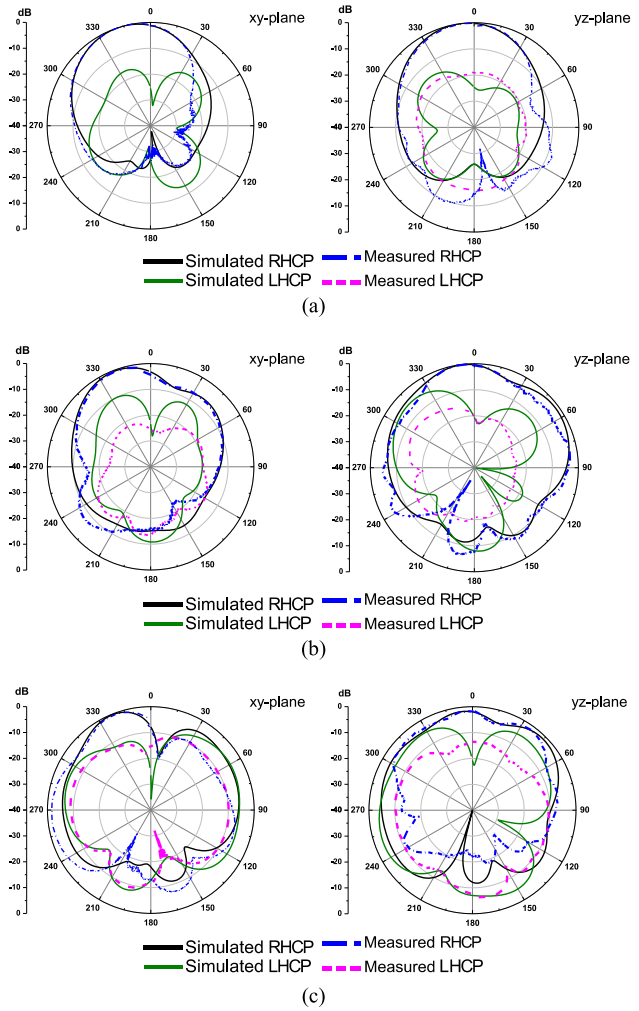

FIGURE 20. Simulated and measured RHCP and LHCP radiation patterns of the proposed multi-shaped metasurface CP patch antenna with parasitic elements at: (a) 3.5 GHz, (b) 4 GHz, (c) 4.5 GHz.

TABLE 2. The existing CMA-characterized metasurface CP patch antennas and the proposed multi-shaped metasurface CP patch antenna with parasitic elements.

Reference	f_c (GHz)	IBW (%)	ARBW (%)	Max. gain (dBic)	Electrical dimension at λ_0
[13]	4	62.5	21	9.04	1.30×1.30×0.040
[14]	5	38.8	14.3	9.4	1.45×1.45×0.074
[15]	8	49.6	33.13	13.17	2.00×2.00×0.080
[28]	5.8	25.08	19.42	8	1.00×1.00×0.058
[29]	7.82	14.7	14.7	8.6	1.30×1.30×0.137
[30]	5.5	28.2	20.9	9.7	1.00×1.00×0.070
[31]	2.15	13.9	17.43	8	0.71×0.71×0.068
[32]	5	29.7	21.4	5.6	0.46×0.46×0.070
[33]	3.5	22.85	8.5	6.5	0.58×0.58×0.043
[34]	2.15	52.5	31.3	7.01	0.71×0.71×0.040
This work	**3.5**	**42.85**	**38**	**7.23**	**1.31×1.31×0.054**

f_c is the center frequency band; and λ_0 is the wavelength at the lowest frequency band.

a complicated feed network and large dimensions. In [28], a single-layered metasurface CP patch antenna achieves narrow IBW and ARBW.

In [29], a rectangular-ring-shaped metasurface CP patch antenna has very narrow IBW and ARBW. In [30], a square-shaped metasurface CP patch antenna with microstrip meander feed line achieves narrow IBW and ARBW while high gain. In [31], a low-profile irregular rectangular-shaped metasurface CP patch antenna has a very narrow IBW and ARBW. In [32], a low-profile multi-shaped metasurface CP sequentially rotated patch antenna achieves narrow IBW and ARBW. In [33], a low-complexity CP patch antenna with corner-truncated metasurface structure achieves a very narrow ARBW.

In [34], a low-profile uniformly metasurface CP patch antenna with dual microstrip feed line and circular-ring slot ground plane achieves wide IBW. However, the antenna requires high-complexity feed network. Unlike the previous works, this research suppresses the non-CP radiation modes by using the multi-shaped metasurface elements (i.e., corner-truncated square-shaped metasurface elements and the metasurface elements of octagonal shape) and the parasitic patches. The multi-shaped metasurface elements and the parasitic patches also improve the IBW and ARBW. As a result, the proposed multi-shaped metasurface CP patch antenna with parasitic elements is suitable for sub-6 GHz 5G NR applications.

IV. CONCLUSION

In this research, a multi-shaped metasurface broadband CP patch antenna with parasitic elements is proposed for 5G NR (sub-6 GHz) applications. The proposed metasurface CP patch antenna involves using triple FR-4 substrate layers stacked together without any air gap. The upper layer contains multi-shaped metasurface elements and corner-truncated square-shaped patches, and the middle layer consists of an L-shaped slot ground plane. The lower layer comprises a microstrip and a fan-shaped stub functioning as the feed line. The design of the proposed metasurface antenna involves four evolutionary stages: Model-I, Model-II, Model-III, and Model-IV, and the surface current distribution and radiation patterns of the four metasurface schemes are analyzed and characterized using CMA.

The CMA results of Model-IV (i.e., the CMA-characterized multi-shaped metasurface CP patch antenna with parasitic elements) show that the modal significance of Modes 1 and 2 are orthogonal, resulting in circular polarization. The non-CP radiation of Modes 3 and 4 of the Model-IV scheme are suppressed by using the multi-shaped metasurface elements (i.e., corner-truncated square-shaped metasurface elements and octagonal-shaped metasurface elements) and the parasitic patches, resulting in wider ARBW. To excite the orthogonal modes, the L-shaped slot (middle layer) is located underneath the intensive magnetic current of the Model-IV scheme. The measured IBW and ARBW are 42.85% and 38%, over the frequency range of 3.4 – 4.9 GHz and 3.27 – 4.6 GHz. The antenna maximum gain is 7.23 dBic at 3.7 GHz. In addition, the comparison of the simulated and measured radiation patterns for RHCP and LHCP are

agreeable. The proposed multi-shaped metasurface CP patch antenna with parasitic elements is therefore functional for 5G NR wireless communication.

REFERENCES

[1] C.-X. Wang et al., "Cellular architecture and key technologies for 5G wireless communication networks," *IEEE Commun. Mag.*, vol. 52, no. 2, pp. 122–130, Feb. 2014.

[2] S. Kumar, A. S. Dixit, R. R. Malekar, H. D. Raut, and L. K. Shevada, "Fifth generation antennas: A comprehensive review of design and performance enhancement techniques," *IEEE Access*, vol. 8, pp. 163568–163593, 2020.

[3] Z. Duan, S. Shen, and G. Wen, "A compact tri-band filtering antenna system for 5G sub-6 GHz applications," *IEEE Trans. Antennas Propag.*, vol. 70, no. 11, pp. 11097–11102, Nov. 2022.

[4] H.-D. Chen, Y.-C. Tsai, C.-Y.-D. Sim, and C. Kuo, "Broadband eight-antenna array design for sub-6 GHz 5G NR bands metal-frame smartphone applications," *IEEE Antennas Wireless Propag. Lett.*, vol. 19, no. 7, pp. 1078–1082, Jul. 2020.

[5] Y. Li, Z. Zhao, Z. Tang, and Y. Yin, "Differentially fed, dual-band dual-polarized filtering antenna with high selectivity for 5G sub-6 GHz base station applications," *IEEE Trans. Antennas Propag.*, vol. 68, no. 4, pp. 3231–3236, Apr. 2020.

[6] Y. Li, Z. Zhao, Z. Tang, and Y. Yin, "Differentially-fed, wide-band dual-polarized filtering antenna with novel feeding structure for 5G sub-6 GHz base station applications," *IEEE Access*, vol. 7, pp. 184718–184725, 2019.

[7] J.-H. Han and N.-H. Myung, "Novel feed network for circular polarization antenna diversity," *IEEE Antennas Wireless Propag. Lett.*, vol. 13, pp. 979–982, 2014.

[8] F. A. Dicandia and S. Genovesi, "A compact CubeSat antenna with beamsteering capability and polarization agility: Characteristic modes theory for breakthrough antenna design," *IEEE Antennas Propag. Mag.*, vol. 62, no. 4, pp. 82–93, Aug. 2020.

[9] J. Zeng, X. Liang, L. He, F. Guan, F. H. Lin, and J. Zi, "Single-fed triple-mode wideband circularly polarized microstrip antennas using characteristic mode analysis," *IEEE Trans. Antennas Propag.*, vol. 70, no. 2, pp. 846–855, Feb. 2022.

[10] N. Supreeyatitikul, T. Lertwiriyaprapa, and C. Phongcharoenpanich, "S-shaped metasurface-based wideband circularly polarized patch antenna for C-band applications," *IEEE Access*, vol. 9, pp. 23944–23955, 2021.

[11] N. Supreeyatitikul, D. Torrungrueng, and C. Phongcharoenpanich, "Quadri-cluster broadband circularly-polarized sequentially-rotated metasurface-based antenna array for C-band satellite communications," *IEEE Access*, vol. 9, pp. 67015–67027, 2021.

[12] J. A. Sheersha, N. Nasimuddin, and A. Alphones, "A high gain wideband circularly polarized antenna with asymmetric metasurface," *Int. J. RF Microw. Comput.-Aided Eng.*, vol. 29. no. 7, Jul. 2019, Art. no. e21740.

[13] N. Supreeyatitikul, P. Janpangngern, T. Lertwiriyaprapa, M. Krairiksh, and C. Phongcharoenpanich, "CMA-based quadruple-cluster leaf-shaped metasurface-based wideband circularly-polarized stacked-patch antenna array for sub-6 GHz 5G applications," *IEEE Access*, vol. 11, pp. 14511–14523, 2023.

[14] C. Zhao and C.-F. Wang, "Characteristic mode design of wide band circularly polarized patch antenna consisting of H-shaped unit cells," *IEEE Access*, vol. 6, pp. 25292–25299, 2018.

[15] X. Gao, S. Yin, G. Wang, C. Xue, and X. Xie, "Broadband low-RCS circularly polarized antenna realized by nonuniform metasurface," *IEEE Antennas Wireless Propag. Lett.*, vol. 21, no. 12, pp. 2417–2421, Dec. 2022.

[16] R. Harrington and J. Mautz, "Theory of characteristic modes for conducting bodies," *IEEE Trans. Antennas Propag.*, vol. 19, no. 5, pp. 622–628, Sep. 1971.

[17] D. Wen, Y. Hao, H. Wang, and H. Zhou, "Design of a wideband antenna with stable omnidirectional radiation pattern using the theory of characteristic modes," *IEEE Trans. Antennas Propag.*, vol. 65, no. 5, pp. 2671–2676, May 2017.

[18] Y. Chen and C.-F. Wang, *Characteristic Modes: Theory and Application to Antenna Engineering*. Hoboken, NJ, USA: Wiley, 2015.

[19] F. H. Lin and Z. N. Chen, "A method of suppressing higher order modes for improving radiation performance of metasurface multiport antennas using characteristic mode analysis," *IEEE Trans. Antennas Propag.*, vol. 66, no. 4, pp. 1894–1902, Apr. 2018.

[20] E. Antonino-Daviu, M. Fabres, M. Ferrando-Bataller, and V. M. R. Penarrocha, "Modal analysis and design of band-notched UWB planar monopole antennas," *IEEE Trans. Antennas Propag.*, vol. 58, no. 5, pp. 1457–1467, May 2010.

[21] B. B. Q. Elias, P. J. Soh, A. A. Al-Hadi, P. Akkaraekthalin, and G. A. E. Vandenbosch, "A review of antenna analysis using characteristic modes," *IEEE Access*, vol. 9, pp. 98833–98862, 2021.

[22] S. Liu, D. Yang, Y. Chen, K. Sun, X. Zhang, and Y. Xiang, "Design of single-layer broadband omnidirectional metasurface antenna under single mode resonance," *IEEE Trans. Antennas Propag.*, vol. 69, no. 10, pp. 6947–6952, Oct. 2021.

[23] Rashmi, A. Kumar, K. Saraswat, and A. Kumar, "Wideband circularly polarized parasitic patches loaded coplanar waveguide-fed square slot antenna with grounded strips and slots for wireless communication systems," *Int. J. Electron. Commun.*, vol. 114, Feb. 2019, Art. no. 153011.

[24] C. A. Balanis, *Antenna Theory Analysis and Design*, 3rd ed. Hoboken, NJ, USA: Wiley, 2005.

[25] A. Sakonkanapong and C. Phongcharoenpanich, "Near-field HF-RFID and CMA-based circularly polarized far-field UHF-RFID integrated tag antenna," *Int. J. Antennas Propag.*, vol. 2020, pp. 1–15, Apr. 2020.

[26] M. A. Sufian, N. Hussain, H. Askari, S. G. Park, K. S. Shin, and N. Kim, "Isolation enhancement of a metasurface-based MIMO antenna using slots and shorting pins," *IEEE Access*, vol. 9, pp. 73533–73543, 2021.

[27] Y. M. Pan, P. F. Hu, X. Y. Zhang, and S. Y. Zheng, "A low-profile high-gain and wideband filtering antenna with metasurface," *IEEE Trans. Antennas Propag.*, vol. 64, no. 5, pp. 2010–2016, May 2016.

[28] A. El Yousfi, A. Lamkaddem, K. A. Abdalmalak, and D. Segovia-Vargas, "A broadband circularly polarized single-layer metasurface antenna using characteristic-mode analysis," *IEEE Trans. Antennas Propag.*, vol. 71, no. 4, pp. 3114–3122, Apr. 2023.

[29] S. Genovesi and F. A. Dicandia, "Characteristic modes analysis of a near-field polarization-conversion metasurface for the design of a wideband circularly polarized X-band antenna," *IEEE Access*, vol. 10, pp. 88932–88940, 2022.

[30] X. Gao, G. Tian, Z. Shou, and S. Li, "A low-profile broadband circularly polarized patch antenna based on characteristic mode analysis," *IEEE Antennas Wireless Propag. Lett.*, vol. 20, no. 2, pp. 214–218, Feb. 2021.

[31] F. A. Dicandia and S. Genovesi, "Characteristic modes analysis of non-uniform metasurface superstrate for nanosatellite antenna design," *IEEE Access*, vol. 8, pp. 176050–176061, 2020.

[32] B. Zheng, N. Li, X. Li, X. Rao, and Y. Shan, "Miniaturized wide-band CP antenna using hybrid embedded metasurface structure," *IEEE Access*, vol. 10, pp. 120056–120062, 2022.

[33] Y. Juan, W. Yang, and W. Che, "Miniaturized low-profile circularly polarized metasurface antenna using capacitive loading," *IEEE Trans. Antennas Propag.*, vol. 67, no. 5, pp. 3527–3532, May 2019.

[34] S. Liu, D. Yang, and J. Pan, "A low-profile broadband dual-circularly-polarized metasurface antenna," *IEEE Antennas Wireless Propag. Lett.*, vol. 18, no. 7, pp. 1395–1399, Jul. 2019.

NATHAPAT SUPREEYATITIKUL (Member, IEEE) received the B.Eng. degree from Mahidol University, Thailand, in 2014, the M.Eng. degree from the King Mongkut's University of Technology Thonburi, Thailand, in 2016, and the D.Eng. degree from the King Mongkut's Institute of Technology Ladkrabang, Thailand, in 2022. His research interests include metasurface, circularly polarized antennas, and MIMO antennas.

TITIPONG LERTWIRIYAPRAPA (Senior Member, IEEE) received the B.S.Tech.Ed. degree in electrical engineering from the King Mongkut's University of Technology North Bangkok in 1996, the M.Eng. degree in electrical engineering from the King Mongkut's Institute of Technology Ladkrabang in 2000, and the M.Sc. and Ph.D. degrees in electrical engineering from The Ohio State University, Columbus, OH, USA, in 2006 and 2007, respectively. He is currently an Associate Professor with the Department of Teacher Training in Electrical Engineering, King Mongkut's University of Technology North Bangkok. His research interests include electromagnetic theory, metamaterial, asymptotic, computational electromagnetics, and hybrid methods. He received the third place in the 2007 USNC/CNC URSI Student Paper Competition, held in Ottawa, Canada, and the Best Paper Award from the 2008 International Symposium on Antennas and Propagation, Taiwan. He was with the Board Committee of the ECTI Association from 2012 to 2015.

NONCHANUTT CHUDPOOTI (Member, IEEE) received the B.Sc. degree (Hons.) in industrial physics and medical instrumentation and the Ph.D. degree in electrical engineering from the King Mongkut's University of Technology North Bangkok, Bangkok, Thailand, in 2012 and 2018, respectively. He was appointed as a Lecturer with the Department of Industrial Physics and Medical Instrumentation, Faculty of Applied Science in 2018. His main research interests include the application of microwave microfluidic sensors, millimeter-wave substrate integrated circuit applications, and substrate integrated waveguide applications. He was a recipient of the Best Presentation Award from the Thailand–Japan Microwave in 2015 and 2018, and the Young Researcher Encouragement Award in 2016.

MONAI KRAIRIKSH (Senior Member, IEEE) was born in Bangkok, Thailand. He received the B.Eng., M.Eng., and D.Eng. degrees in electrical engineering from the King Mongkut's Institute of Technology Ladkrabang (KMITL), Thailand, in 1981, 1984, and 1994, respectively. He was a Visiting Research Scholar with Tokai University in 1988, and with the Yokosuka Radio Communications Research Center, Communications Research Laboratory in 2004. He worked as the Director of the Research Center for Communications and Information Technology from 1997 to 2002. He joined KMITL and is currently a Professor with the Department of Telecommunication Engineering. His main research interests include antennas for wireless communications and microwaves in agricultural applications. He was the Chairperson for the IEEE MTT/AP/Ed Joint Chapter in 2005 and 2006. He served as the General Chairperson of the 2007 Asia–Pacific Microwave Conference, and an Advisory Committee of the 2009 International Symposium on Antennas and Propagation. He served as a Distinguished Lecturer for the IEEE Antennas and Propagation Society from 2012 to 2014. He was the President of the Electrical Engineering/Electronics, Computer, Telecommunications and Information Technology Association in 2010 and 2011, and was the Editor-in-Chief of the *ECTI Transactions on Electrical Engineering, Electronics, and Communications*. He was recognized as a Senior Research Scholar of the Thailand Research Fund in 2005 and 2008, and a Distinguished Research Scholar of the National Research Council of Thailand.

CHUWONG PHONGCHAROENPANICH (Member, IEEE) received the B.Eng. (Hons.), M.Eng., and D.Eng. degrees from the King Mongkut's Institute of Technology Ladkrabang (KMITL), Bangkok, Thailand, in 1996, 1998, and 2001, respectively. He is currently a Professor with the Department of Telecommunications Engineering, KMITL, where he also serves as the Leader of Innovative Antenna and Electromagnetic Applications Research Laboratory. His research interests include antenna design for various mobile and wireless communications, conformal antennas, and array antenna theory. He has served as the Chair for the IEEE MTT/AP/ED Thailand Chapter from 2014 to 2018. He has been on the organizing committee of several international conferences, including the TPC Chair of 2009 International Symposium on Antennas and Propagation (ISAP) and a TPC member of ISAP 2012. He is also a Reviewer of many scientific journals, including the IEEE TRANSACTIONS ON ANTENNAS AND PROPAGATION, IEEE ACCESS, *IET Microwaves, Antennas and Propagation*, *Electronics Letters*, and *ECTI Transactions*, and many international conferences, including ISAP and APMC. He was on the Board Committee of ECTI Association from 2008 to 2011 and 2014 to 2015. He was an Associate Editor of the *IEICE Transactions on Communications* and the *ECTI Transactions on Electrical Engineering, Electronics, and Communications*. He is also an Associate Editor of the *IEICE Communications Express*. He is also a Senior Member of IEICE and a member of ECTI.